Evolution kinetics of elementary point defects in ZnO implanted with low fluences of helium at cryogenic temperature

C. Bhoodoo,[*] A. Hupfer, L. Vines, E. V. Monakhov, and B. G. Svensson

University of Oslo, Department of Physics, Center for Materials Science and Nanotechnology, P.O. Box 1048 Blindern, N-0316 Oslo, Norway

Hydrothermally grown n-type ZnO samples, implanted with helium (He$^+$) at a sample temperature of $\sim$40 K and fluences of 5×10^9 and 5×10^{10} cm^{-2}, have been studied *in situ* by capacitance voltage (CV) and junction spectroscopy measurements. The results are complemented by data from secondary ion mass spectrometry and Fourier transform infrared absorption measurements and first-principles calculations. Removal/passivation of an implantation-induced shallow donor center or alternatively growth of a deep acceptor defect are observed after annealing, monitored via charge carrier concentration (N_d) versus depth profiles extracted from CV data. Isothermal anneals in the temperature range of 290–325 K were performed to study the evolution in N_d, revealing a first-order kinetics with an activation energy, $E_a \approx 0.7$ eV and frequency factor, $c_0 \sim 10^6$ s^{-1}. Two models are discussed in order to explain these annealing results. One relies on transition of oxygen interstitials (O$_i$) from a split configuration (neutral state) to an octahedral configuration (deep double acceptor state) as a key feature. The other one is based on the migration of Zn interstitials (double donor) and trapping by neutral Zn-vacancy-hydrogen complexes as the core ingredient. In particular, the latter model exhibits good quantitative agreement with the experimental data and gives an activation energy of $\sim$0.75 eV for the migration of Zn interstitials.

I. INTRODUCTION

Understanding intrinsic defects and their role for the electrical conductivity of semiconducting oxides is essential for further materials development targeting efficient optoelectronic devices. However, isolated elementary point defects, i.e., interstitials (I) and vacancies (V), are often highly mobile and challenging to characterize. This holds particularly for zinc oxide (ZnO), where, e.g., the interstitial zinc (Zn$_i$) is theoretically expected to have an activation energy for migration of only $\sim$0.5 eV [1], making it mobile at, and even below, room temperature (RT) [2–4]. Due to the high mobility of Zn$_i$, recombination with V_{Zn} is prominent during electron irradiation and ion bombardment, but in spite of high dynamic annealing rates, residual disorder remains in the zinc sublattice as well as in the oxygen sublattice (V_O,O$_i$) [5,6]. For implantation (or irradiation) at cryogenic temperatures, the displaced crystal atoms possess low thermal energy to enable migration and reactions with other defects (or impurities). Hence, low temperature implantation with *in situ* characterization provides an opportunity to study primary defects and their electrical/optical/structural properties as well as thermal stability.

Most of the primary defects in ZnO are electrically active, where Zn$_i$ is a shallow double donor, the zinc vacancy (V_{Zn}) is a deep double acceptor, and the oxygen vacancy (V_O) is a double donor (negative U) with the $++/0$ thermodynamic transition occurring at least 1 eV below the conduction band edge (E_c), as estimated by calculations using density-functional theory (DFT) [7,8]. The interstitial oxygen (O$_i$) can be found in both a split and octahedral configuration, where O$_i$ (split) is electrically neutral, while O$_i$ (oct) is a deep double acceptor [1].

For studying and understanding electrically active defects, both intrinsic and impurity related ones, deep level transient spectroscopy (DLTS) is one of the most sensitive analysis techniques. Several RT irradiation studies of ZnO using DLTS have been reported [9–13]. In particular, it has been found that a redistribution of defects occurs below 400 K, indicating a high mobility, consistent with an efficient dynamic annealing but possibly also with the formation of large and more stable defect clusters. However, there are very few low temperature irradiation studies of ZnO reported in the literature, with the exception of *in situ* electron paramagnetic resonance (EPR) studies after MeV electron irradiation at 4.2 K by Gorelkinskii and Watkins [2], and Vlasenko and Watkins [3].

Here, we report on the evolution kinetics of an electrically active elementary point defect in monocrystalline ZnO samples, implanted with low fluences of helium ions (He$^+$) at a temperature of $\sim$40 K. Charge carrier concentration (N_d) versus depth profiles extracted from *in situ* capacitance voltage (CV) measurements reveal only a modest effect on N_d immediately after the implantation, but then a gradual reduction occurs with increasing time and temperature. Two different kinetics models are discussed in detail, and especially, the one involving migration of Zn$_i$ and reaction with hydrogen-passivated Zn vacancies (H$_2V_{Zn}$) exhibits a close quantitative agreement with the experimental data.

II. EXPERIMENTAL AND THEORETICAL APPROACH

Wafers of hydrothermally grown n-type ZnO (HT-ZnO) purchased from Tokyo Denpa were cut into 5×5 mm^2 sized samples. The samples were cleaned in ultrasonic bath using acetone followed by isopropanol, for 5 min each. After a 40 s treatment in boiling H$_2$O$_2$ (31%), 150-nm-thick palladium Schottky contacts with a diameter of 1 mm were deposited on the Zn-polar face using electron-beam evaporation and a shadow mask. 20 nm of titanium followed by 50 nm

---

[*]chidanand.bhoodoo@fys.uio.no

of aluminum (Al) were electron-beam evaporated for back side Ohmic contacts. The Schottky contacts (SC) showed a current rectification of approximately four orders of magnitude between reverse and forward bias (-2 V and $+2$ V). The SC were wire bonded to the measurement terminals using a 30-μm-diameter gold wire, minimizing shadowing during implantation. The samples were loaded into a vacuum chamber connected to a 1 MV NEC Tandem accelerator beam line and equipped with a closed-cycle helium cryostat (25–350 K). The samples were then cooled down and implanted at a temperature of $\sim$40 K with 750–900 keV He$^+$ ions, having a projected range (R_p) of $\sim$1.8 μm, as estimated by Monte Carlo simulations using the SRIM code [14], and fluences ranging from $\sim$5 × 10^9 to $\sim$5 × 10^{10} cm^{-2}.

After implantation, the samples were heated in the on-line chamber to a desired annealing temperature while undertaking either thermal admittance spectroscopy (TAS) or DLTS measurements. TAS was conducted using an Agilent 4284A precision LCR meter (20 Hz to 1 MHz), while DLTS was performed using a 1 MHz Boonton 7200 capacitance meter, an Agilent 81104A 80 MHz pulse generator, and a Lake-shore 332 temperature controller. A Keithley 6487 picoammeter was used to record the current voltage characteristics. The setups were controlled by a LABVIEW program run from a desktop computer via a GPIB interface and a data acquisition card. For the DLTS measurements, a reverse bias of -7 V was applied with a filling pulse of 7 V and 50 ms duration. DLTS spectra with rate windows from (20 ms)$^{-1}$ to (5.12 s)$^{-1}$ were extracted from the recorded transients using lock-in and GS4 type weighting functions [15]. CV data at probing frequencies varying from 1 kHz to 1 MHz were also recorded at specific temperatures while heating up the samples to the desired annealing temperature. After the heating up, the samples were isothermally annealed at temperatures in the range of 290–325 K for durations reaching 300 h while continuously monitoring the N_d profiles via CV measurements. Subsequently, the samples were transferred to an off-line DLTS setup where high temperature DLTS and CV measurements were performed.

Chemical characterization was carried out by secondary ion mass spectrometry (SIMS) using a Cameca IMS 7f instrument with a primary beam of 10 keV O$_2^+$ ions. The impurity concentrations were calibrated using implanted reference samples. The crater depths were measured with a Dektak 8 stylus profilometer and a constant erosion rate as a function of sputtering time was assumed.

For selected samples, Fourier transform infrared (FTIR) absorption spectra were recorded with a Bruker IFS125 HR spectrometer equipped with a Globar light source, a CaF$_2$ beam splitter, and an InSb detector. The measurements were performed at 20 K with a spectral resolution of 0.5 cm^{-1}. Unpolarized light was used with the wave vector, k, directed perpendicular to the c axis of the samples.

DFT calculations of defect formation energies were undertaken using the plane-wave projector augmented-wave method [16] with the Perdew-Burke-Ernzerhof generalized gradient approximations functional [17] as implemented in the VASP code [18]. The calculations were performed using 128 atom supercells, a 400 eV cutoff energy, and eight k points. The initial geometries were relaxed until the Feynman-Hellmann forces were below 50 meV/Å. Defect reaction pathways were
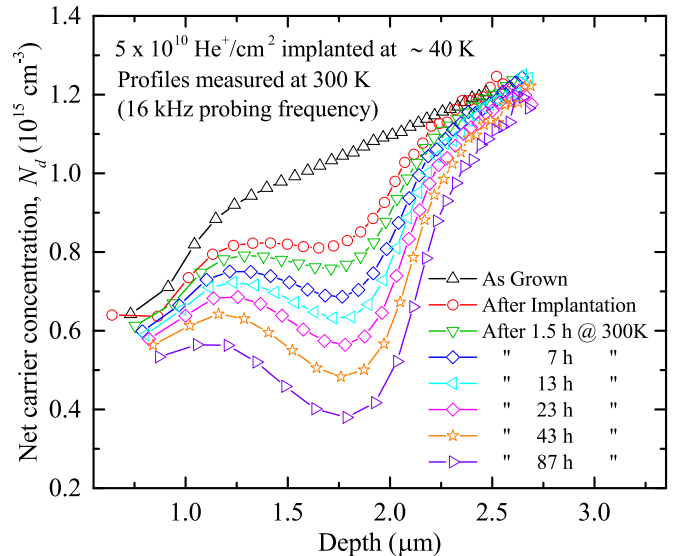

FIG. 1. N_d versus depth profiles with increasing time at 300 K after implantation at $\sim$40 K. The profiles were measured using 16 kHz probing frequency.

determined using the climbing-image nudged-elastic-band (NEB) method, as implemented by Henkelman *et al.* [19]. For calculation of O$_i$ configuration transition energies, the Heyd-Scuseria-Ernzerhof (HSE) functional [20] was applied with 37.5% Hartree-Fock mixing, which reproduces the experimental band gap of ZnO. For these calculations, the cutoff energy was reduced to 300 eV and only the Γ point was used. However, for selected geometries, calculations were also performed with a cutoff energy of 400 eV yielding a relative difference of less than 3% in the total energy values compared to those obtained with the 300 eV cutoff energy. The transition energies were determined assuming the geometries given by the NEB calculations. Finally, the transition energies were corrected for finite supercell size using the method of Kumagai *et al.* [21,22].

III. RESULTS

A. Electrical measurements

Figure 1 shows the evolution of the N_d versus depth profiles at 300 K in a sample before and after implantation, and after subsequent annealing at 300 K. The profiles were extracted from CV measurements performed at 300 K using a 16 kHz probing frequency. The sample was implanted at $\sim$40 K with 850 keV He$^+$ ions, and a fluence of $\sim$5 × 10^{10} cm^{-2}. The profile prior to the implantation shows a weak increase with depth from $\sim$1.0 × 10^{15} cm^{-3} at 1.3 μm to 1.2 × 10^{15} cm^{-3} at 2.5 μm. A reduction in N_d by $\sim$20% occurs close to R_p after the implantation, which evolves further during the subsequent annealing. After 87 h at 300 K, the reduction is more than 60%. A similar and even more pronounced loss in N_d has also been observed in previous studies after self-ion implantations performed at RT [9].

Figure 2(a) shows N_d profiles obtained at 200, 300, and 400 K, using 1 MHz probing frequency, in a sample implanted with $\sim$5 × 10^9 He$^+$/cm^2 at $\sim$40 K and then annealed at
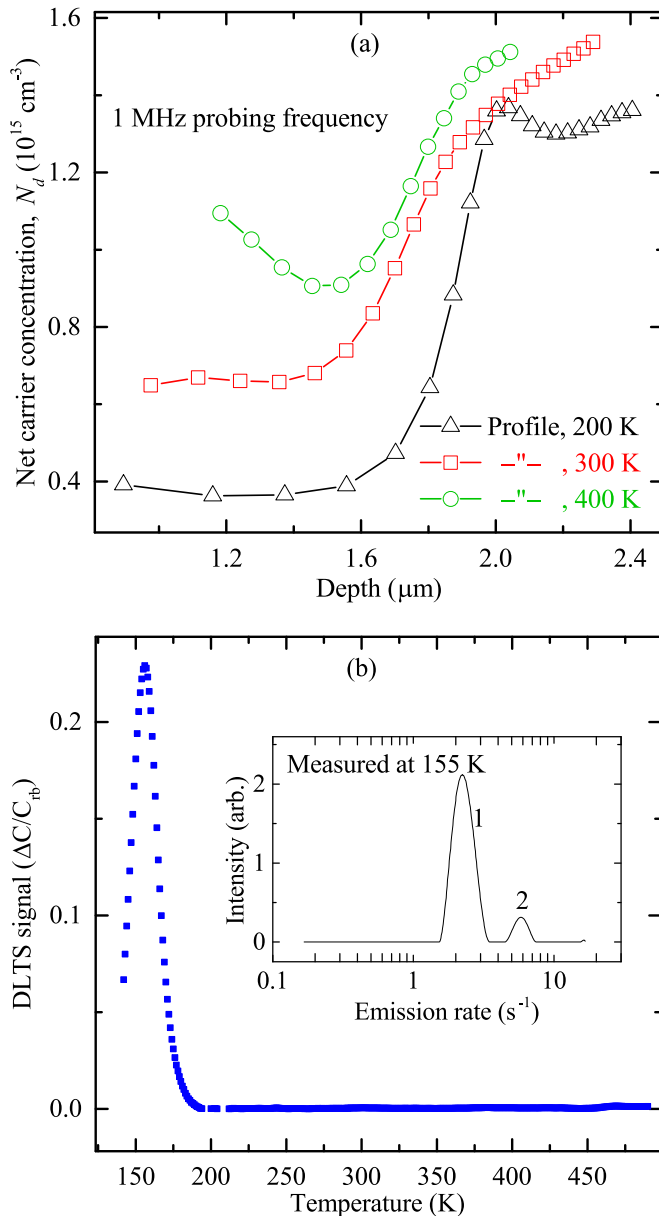
FIG. 2. (a) N_d profiles, 1 MHz probing frequency, recorded at different temperatures for a sample implanted with $\sim 5 \times 10^9$ He$^+$/cm^2 at ~ 40 K and then annealed at 325 K for 150 h. The profile at 400 K was recorded off line. (b) DLTS spectrum of the sample in (a), rate window = (640 ms)$^{-1}$. The inset shows the Laplace DLTS spectrum recorded at 155 K, displayed as signal intensity versus emission rate (s^{-1}).

325 K for 150 h. An increase in the concentration of responding charge carriers is found at 400 K but a considerable amount of the reduction in N_d at $\sim R_p$ still persists ($\sim 5 \times 10^{14}$ cm^{-3}). It should also be emphasized that no annealing takes place during the 400 K measurements; the N_d profiles recorded at 300 K (and at lower temperatures) before and after the 400 K measurements were identical. An anomalous overshoot occurs beyond R_p in the profile recorded at 200 K, which is unambiguous evidence of the presence of a deep acceptor center with a nonuniform depth distribution [23]. The overshoot is found in profiles acquired between ~ 140 K

and ~ 260 K, i.e., when the emission rate from the acceptor level is intermediate to the sweep frequency and the probing frequency of the CV measurements [23,24]. On the basis of these results, the position of the acceptor level is estimated to be ~ 0.3 eV below the conduction band edge (E_c) and it exhibits a rather moderate concentration below $\sim 2 \times 10^{14}$ cm^{-3}. Hence, this level is not anticipated to play a dominant role for the observed reduction in N_d, which is also corroborated by CV measurements undertaken at elevated temperatures, like the 400 K profile in Fig. 2(a). At these temperatures, the charge carriers trapped by the $\sim E_c - 0.3$ eV level respond to the probing frequency (1 MHz) but a strong reduction in N_d remains. Accordingly, the main loss in N_d arises from either a compensating defect with an acceptor level located very deep in the band gap, possibly in the lower part, and/or passivation/removal of a shallow donor dopant.

Figure 2(b) shows the DLTS spectrum of the $\sim 5 \times 10^9$ He$^+$/cm^2 implanted sample [rate window = (640 ms)$^{-1}$]. Only the so-called E3 level is detected, with a position of $\sim E_c - 0.3$ eV [10]. E3 is generally regarded to be donorlike [25,26] and involves hydrogen [26]. However, in a comprehensive DLTS study of point defects in ZnO, Mtangi *et al.* [27] have shown that the E3 peak may contain more than one contribution and the presence of an acceptorlike level cannot be excluded. Indeed, high energy resolution Laplace DLTS measurements of the E3 level in our samples reveal the presence of two contributions, as illustrated by the inset of Fig. 2(b) showing a spectrum recorded at 155 K. The two contributions are close in energy position with a difference of only ~ 20 meV, as deduced from Arrhenius analysis of six Laplace spectra acquired between 155 and 190 K. Further, the high emission rate peak, labeled 2 in the inset, contributes to the total E3 peak concentration by $\sim 25\%$, which agrees closely with the absolute concentration of $\sim 1 \times 10^{14}$ cm^{-3} estimated for the deep acceptorlike level giving rise to the anomalous overshoot in Fig. 2(a). The remaining 75% of the E3 concentration arises from the peak 1 and is due to the "ordinary" donorlike level of E3.

The absence of any peaks in the DLTS spectrum in Fig. 2(b) above 200 K and up to the maximum temperature scanned, 500 K, implies that any deep acceptor level causing a major compensation of N_d must be located at least 1.0 eV below E_c, assuming a typical value of $\sim 10^{-15}$ cm^2 for the electron capture cross section.

In order to study the evolution kinetics of N_d, isothermal anneals in the temperature range of 290–325 K were performed. Figure 3 shows the loss in N_d versus annealing time at 300 and 325 K for two samples implanted with different fluences. N_d (loss) is given by the difference between the N_d value in the as-grown sample and the remaining one at R_p, after a given anneal time. The CV measurement parameters used were similar to those in Fig. 1, and the sample temperature was 260 K. The probing frequency, 16 kHz, is slow enough to enable charge carriers trapped by the E3 center to respond and contribute to the capacitance recorded. In contrast, any deep acceptor level will remain occupied and not follow the probing frequency. Initially, N_d (loss) increases rapidly with the annealing time, Fig. 3, but then saturates after ~ 150 h. Interestingly, the growth rate of N_d (loss) increases not only with the temperature but also with the implantation fluence, as
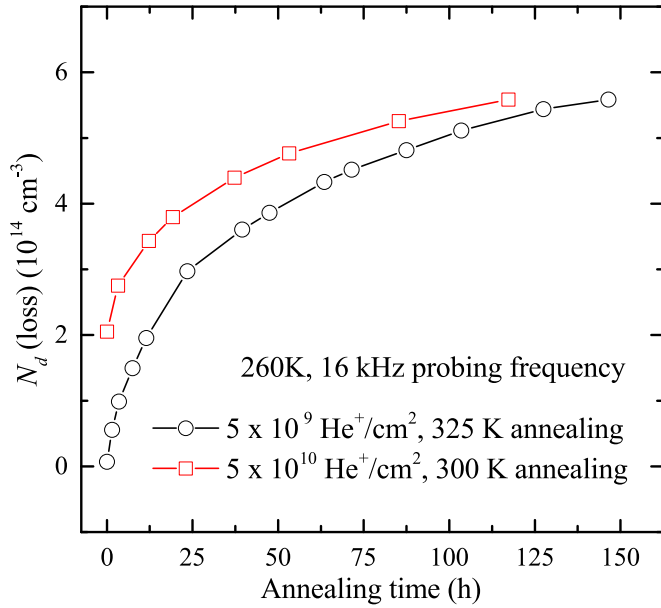
FIG. 3. N_d (loss), given by the difference between the as-grown charge carrier concentration and the remaining one at R_p, versus annealing time for two samples implanted with different fluences at $\sim$40 K and then annealed at 300 and 325 K, respectively.

illustrated in Fig. 3 where the growth rate in the high-fluence sample (5×10^{10} cm^{-2}) is higher than that in the low-fluence one (5×10^{9} cm^{-2}) despite a lower annealing temperature (300 K versus 325 K). However, the saturation concentration of N_d (loss) remains constant within less than $\sim$10%, irrespective of the implantation fluence used.

As shown in Fig. 4(a) for samples implanted with the fluence of 5×10^{10} cm^{-2}, the evolution of N_d (loss) with annealing time can be described by

$$[N_d(\text{loss})] = [N_d(\text{saturated loss})](1 - e^{-c(T)t}), \quad (1)$$

where N_d (saturated loss) is the saturated concentration of N_d (loss) and $c(T)$ is a temperature dependent rate constant and t is the annealing time. That is, first-order reaction kinetics applies for N_d (loss) and the $c(T)$ values, extracted by least-squares linear fits of the data in Fig. 4(a), exhibit an Arrhenius behavior:

$$c(T) = c_0 e^{-E_a/kT}, \quad (2)$$

where T is the absolute temperature, k is Boltzmann's constant, E_a is the thermal activation energy of the process, and c_0 is the preexponential factor. The $c(T)$ values obtained are depicted versus $1000/T$ in Fig. 4(b) and values of 0.69 ± 0.04 eV and $\sim 1.3 \times 10^{6}$ s^{-1} are deduced for E_a and c_0, respectively.

The c value determined for the 5×10^{9} cm^{-2} fluence sample annealed at 325 K (cf. Fig. 3) is also included in Fig. 4(b) and multiplied by a factor of 10. Within the experimental accuracy, this value agrees with that extrapolated from the Arrhenius dependence of the c values for the 5×10^{10} cm^{-2} fluence samples. Hence, a one-to-one proportionality appears to hold between the rate constant and the ion fluence.
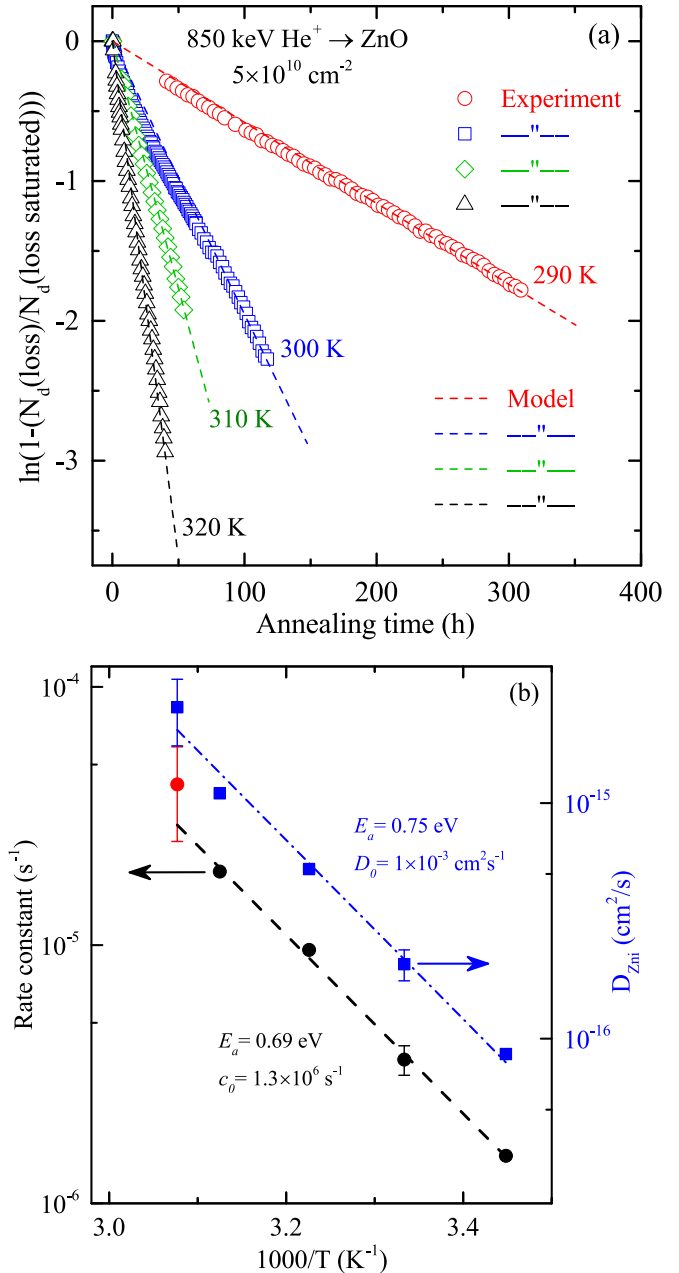

FIG. 4. (a) $\ln[1 - (\frac{N_d(\text{loss})}{N_d(\text{saturated loss})})]$ versus annealing time at 290, 300, 310, and 320 K for samples implanted with $\sim$5 $\times$ 10^{10} He$^+$/cm^2 at $\sim$40 K. The dotted lines represent results from simulations using the model outlined in Sec. IV C. (b) Arrhenius plot of the reaction rate constant determined experimentally versus the reciprocal absolute annealing temperature. The black circles represent values obtained by least-squares fits of the data in Fig. 4(a) (ion fluence = 5 $\times$ 10^{10} cm^{-2}), while the red circle shows the value obtained from samples implanted with a fluence of 5×10^{9} cm^{-2} and annealed at 325 K. The latter value is multiplied by a factor of 10 and is not included in the fit yielding an activation energy of 0.69 eV with a prefactor of 1.3×10^{6} s^{-1}. The blue squares (right y axis) show values of the Zn$_i$ migration (D_{Zn_i}) deduced from the model simulations in Sec. IV C. Error bars indicate the experimental accuracy (10%–20%).

TABLE I. Impurity concentrations determined by SIMS.

Samples Annealed T (K)	Al (cm^{-3})	In (cm^{-3})	Li (cm^{-3})
300	~1.5×10^{15}	~3.9×10^{15}	~1.8×10^{17}
310	~1.4×10^{15}	~4.8×10^{15}	~1.8×10^{17}
320	~2.0×10^{15}	~8.4×10^{15}	~1.8×10^{17}
325	~1.7×10^{15}	~3.7×10^{15}	~1.8×10^{17}

B. SIMS measurements

According to mass spectra acquired for the studied samples, the most prominent residual impurities are found to be Al, indium (In), and lithium (Li). Their concentrations have been quantified by depth-profiling measurements showing uniform distributions and the values are given in Table I. Li is clearly the most abundant impurity reading values in the low 10^{17} cm^{-3} range. Further, hydrogen (H) is also present in the samples, as evidenced by the large E3 peak in the DLTS spectra, Fig. 2(b), but below the detection limit of the SIMS measurements (~5×10^{17} cm^{-3}). The same holds for nitrogen (N), also having a detection limit of ~5×10^{17} cm^{-3}.

IV. DISCUSSION

A. Loss in N_d and the role of primary intrinsic defects

Helium is a light and inert species and after low fluences He$^+$ implantations at cryogenic temperatures, intrinsic point defects will prevail, i.e., Zn$_i$, V_{Zn}, O$_i$, and V_O. Immediately after the implantation, only modest loss in N_d occurs showing a balance for each pair of sublattice defects. For the Zn sublattice, Zn$_i$ is anticipated to act as a shallow double donor (Zn$_i{}^{2+}$) while V_{Zn} is a deep double acceptor ($V_{Zn}{}^{2-}$) [7,8], and in the studied samples, having a Fermi-level position of ~$E_c - 0.2$ eV at RT, Zn$_i$ and V_{Zn} are in the 2+ and 2− charge states, respectively. For the O sublattice, V_O has been extensively studied both theoretically and experimentally [7,8,28–30], and it is a negative-U defect of double-donor character. The thermodynamic transition between the neutral and the 2+ charge state takes place rather deep in the band gap at ~$E_c - 1.0$ eV, and $V_O{}^0$ dominates in the studied samples at RT. O$_i$, on the other hand, can exist both in a split configuration (O$_i$ (split)) and in an octahedral one (O$_i$ (oct)) [1] where the former is electrically neutral and the latter a deep double acceptor. The modest loss in N_d immediately after implantation shows that O$_i$ (split) must be the dominant configuration. Transformation from O$_i$ (split) to O$_i$ (oct) may occur during the subsequent annealing and this is discussed in Sec. IV B as a possible process for the loss in N_d.

In principle, two main types of processes can account for the loss in N_d: (i) formation of excess deep acceptors, such as O$_i$ (oct), compensating the shallow donor(s), and (ii) removal/passivation of the shallow donor(s) through reactions with other impurities or defects such that the net excess of free electrons decreases. In (ii), one could also suspect out-diffusion of the generated Zn$_i$'s from the implanted region, driven by the concentration gradient, since Zn$_i$ is regarded as mobile at RT with a theoretically estimated activation energy for migration of only ~0.5–0.8 eV [1]. However, this suspicion

does not comply with the experimentally observed first-order kinetics of the evolution of N_d (loss) and that the saturation value of N_d (loss) exhibits no dependence on the ion fluence. Further, the CV profiles reveal no increase in N_d outside the implanted region and their shape stays about the same during the course of annealing (cf. Fig. 1).

The proportionality between the loss rate constant, c, and the He$^+$ fluence shows a direct involvement of an implantation-induced defect in the loss process of N_d. Moreover, there are basically three kinds of physical processes giving rise to first-order kinetics (see Ref. [31], and references therein): (a) dissociation/transformation where a species A disintegrates/transforms into new "constituents" while back reactions are weak, (b) a reaction of species A with a species B where the concentration of B is much higher than that of A, and (c) a reaction between A and B where B is continuously replenished by a source such that the concentration of B remains constant as a function of time. The processes (a) and (b) are applicable to our case, while (c) is merely valid for studies of defect injection from an infinite source [32]. According to our SIMS, DLTS, and FTIR data, Al, In, and H are the main impurities as candidates for shallow donors in the studied samples. They all give rise to donor states at ~40–50 meV below E_c, in the configurations of Al$_{Zn}$, In$_{Zn}$, and H$_O$/H$_i$ [8,25,33,34], which is consistent with the TAS results obtained for the present samples (not shown). Among the primary intrinsic defects, Zn$_i$ and O$_i$ are sufficiently mobile in the temperature range 290–325 K to account for the measured evolution of N_d, while V_{Zn} and especially V_O are practically immobile with predicted migration energies of ~1.4 and ~2.4 eV, respectively [1]. However, a direct interaction of Zn$_i$ and O$_i$ with the shallow donor impurities does not reduce the net electron concentration, e.g., Zn$_i{}^{2+}$ + Al$_{Zn}{}^+$(In$_{Zn}{}^+$) → Zn$_{Zn}{}^0$ + Al$_i{}^{3+}$(In$_i{}^{3+}$) and O$_i$ + H$_O{}^+$ → O$_O$ + H$_i{}^+$ have no net effect on N_d. In addition, the Coulomb repulsion between Zn$_i{}^{2+}$ and the shallow donors strongly suppresses the probability of these reactions. In spite of Coulomb attraction, similar arguments hold also for the reactions Zn$_i{}^{2+}$ + Li$_{Zn}{}^-$ → Zn$_{Zn}$ + Li$_i{}^+$ and Zn$_i{}^{2+}$ + Li$_{Zn}$H → Zn$_{Zn}$ + Li$_i{}^+$ + H$_i{}^+$ with Li$_{Zn}$ being a (deep) acceptor and Li$_i$ a (shallow) donor. Hence, in order to interpret the experimental data more elaborate scenarios are required and in the following sections (Secs. IV B and IV C), two possible ones will be discussed. The first utilizes O$_i$ as a crucial ingredient with the kinetics given by a process of type (a). The second is based on the migration of Zn$_i{}^{2+}$ and subsequent annihilation with preexisting (neutral) H$_2V_{Zn}$ complexes in the samples, leading to a loss in N_d with the kinetics given by a process of type (b). Especially, the second model is shown to give close quantitative agreement with the experimental data.

B. Transformation of O$_i$ from split to octahedral configuration

As discussed in Sec. IV A, immediately after the implantation O$_i$ (split) is the predominant O$_i$ configuration being electrically inactive and yielding no loss in N_d. This conclusion is further corroborated by results from the DFT calculations; the inset of Fig. 5 displays the calculated relative formation energy of O$_i$ for E_F fixed at 3 eV as a function of the reaction coordinate, r, when transforming between the split
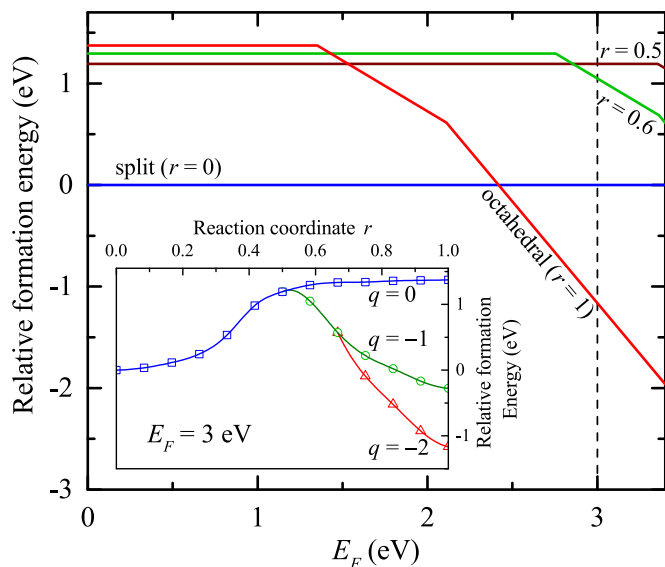
FIG. 5. Relative formation energies as a function of Fermi level (E_F) position for O_i in split position (reaction coordinate $r = 0$), octahedral position ($r = 1$), and transition geometries ($0 < r < 1$) in ZnO. E_F equal to zero corresponds to the valence-band maximum. Only segments corresponding to the lowest-energy charge states are shown. The slope of these segments indicates the charge state. Kinks in the curves indicate transitions between different charge states. The inset shows the relative formation energy as a function of r for E_F fixed at 3 eV.
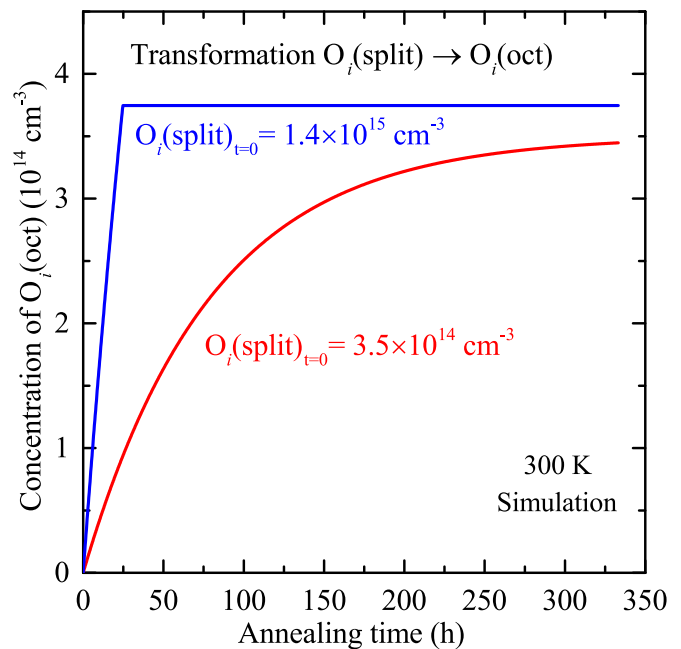

FIG. 6. Simulation results for the evolution of interstitial oxygen atoms in the octahedral configuration as a function of annealing time at 300 K employing the model outlined in Sec. IV B. Results are shown for two initial concentrations of O_i (split) at $t = 0$.

and octahedral configurations. The latter is electrically active, acting as double deep acceptor. The left y axis refers to the O_i (split) ($r = 0$), while the right y axis to O_i (oct) ($r = 1$). The blue curve is the relative formation energy of neutral ($q = 0$) O_i, and the green and red parts ($r > 0.5$) are for O_i with charge states $q = -1$ and $q = -2$, respectively. The transformation is asymmetric and occurs at r closer to O_i (oct) ($r > 0.5$), i.e., O_i (split) is the most likely configuration during a random generation process such as ion implantation.

Figure 5 shows the calculated relative formation energy of O_i at four different reaction coordinates: $r = 0$ (O_i (split)), $r = 1$ (O_i (oct)), and two transition geometries, $r = 0.5$ and 0.6, versus the position of E_F. O_i (oct)$^{2-}$ is favorable in our samples, $E_F \approx E_c - 0.2$ eV, and as disclosed by the inset, an energy barrier of ~ 1.2 eV is obtained for the O_i (split) to O_i (oct)$^{2-}$ transformation. This value is in fair agreement with the measured activation energy of ~ 0.7 eV for the loss of N_d. On the other hand, the experimental value of $\sim 10^6$ s^{-1} for the preexponential factor, c_0, of the rate constant does not comply with the attempt frequency of an "ordinary" transformation process, typically in the range of 10^{13} s^{-1} [35]. Hence, another process must be controlling c_0 and a possible candidate is the electron filling of the O_i (oct) acceptor states, i.e., the transfer rate is limited by the rate of electron capture to these states. Indeed, adopting the description by Shockley-Read-Hall [36,37] and omitting any change in entropy, the rate of electron capture by an unoccupied state in the band gap can be expressed as

$$c_n = \sigma_n \langle v_{th} \rangle n, \qquad (3)$$

where σ_n is the electron capture cross section, $\langle v_{th} \rangle$ is the average thermal electron velocity, and n is the free electron concentration. Putting n equal to N_d ($\sim 1 \times 10^{15}$ cm^{-3}), $\langle v_{th} \rangle \approx 10^7$ cm/s at RT, and $\sigma_n \approx 10^{-15}$–$10^{-16}$ cm^2, which is a typical range for the capture cross section of acceptorlike defects, one obtains $c_n \approx 10^6$–10^7 s^{-1}, in good correspondence with the experimental c_0 value.

Further, the growth rate of [O_i (oct)] (brackets denote concentration) will scale with the ion fluence since

$$\frac{d[O_i(\text{oct})]}{dt} = -\frac{d[O_i(\text{split})]}{dt} = c[O_i(\text{split})], \qquad (4)$$

with [O_i (split)] being proportional to the ion fluence. However, in order to account for the lack of fluence dependence of N_d (saturated loss), also the reverse transformation (O_i (oct)$^{2-} \rightarrow O_i$ (split)) needs to be regarded. Initially, the rate constant of the reverse transformation should be low, otherwise first-order kinetics will not apply for the loss of [O_i (split)], and then increase rapidly as [O_i (oct)$^{2-}$] approaches $\frac{1}{2} \times N_d$ (saturated loss) (the factor $\frac{1}{2}$ arises because of the $2-$ charge state). Such a behavior can be inferred from Fig. 5 with the energy barrier for the O_i (oct)$^{2-} \rightarrow O_i$ (split) transformation decreasing gradually as [O_i (oct)$^{2-}$] grows, shifting the E_F position deeper into the band gap. Eventually, the shift in E_F becomes sufficient to equalize the formation energies of the two O_i configurations. This leads to steady state between the two transfer rates and [O_i (oct)$^{2-}$] saturates.

Figure 6 illustrates an example of simulated results for the growth of [O_i (oct)$^{2-}$] as a function of annealing time at 300 K. Two different initial concentrations of O_i (split) are assumed with a relative difference by a factor of 4 and where the lower one is given by the limit set by N_d (saturated loss) observed experimentally ($\sim 6 \times 10^{14}$ cm^{-3}). Moreover, the initial

barrier height for the O_i (oct)$^{2-}$ → O_i (split) transformation is taken as 1.2 eV, guided by the DFT results in Fig. 5, with a preexponential factor of 10^9 s^{-1} for the rate constant. For the O_i (split) → O_i (oct)$^{2-}$ transformation, the experimental values with an energy barrier of ∼0.7 eV and a frequency factor of 10^6 s^{-1} are used [cf. Fig. 4(b)]. In the case of the low $[O_i$ (split)$]_{t=0}$, the barrier for O_i (oct)$^{2-}$ → O_i (split) decreases by less than ∼0.05 eV and the rise in $[O_i$ (oct)$^{2-}]$ follows ordinary first-order kinetics with negligible influence by the reverse transformation. In contrast, for the high $[O_i$ (split)$]_{t=0}$ the O_i (oct)$^{2-}$ → O_i (split) barrier decreases by more than 0.3 eV and the rise in $[O_i$ (oct)$^{2-}]$ is rapidly terminated at a saturation level similar to that for the low $[O_i$ (split)$]_{t=0}$ case (see Fig. 6). Here, it should be underlined that the values used for the barrier height and preexponential factor of the O_i (oct)$^{2-}$ → O_i (split) transition are not unique and other combinations can yield similar behavior but with the constraint of an initial energy barrier between 0.9 and 1.5 eV.

Semiquantitatively, the simulation results in Fig. 6 reproduce the main experimental findings: first-order kinetics with a low prefactor for the evolution of N_d (loss), a reaction rate constant being proportional to the ion fluence, and a saturation value of N_d (loss) with a weak (if any) dependence on the ion fluence. However, especially the latter finding is challenging to fulfill given the net doping concentration N_d of the samples and the ion fluences employed. In Fig. 6, "only" a factor of 4 is assumed for the relative variation in $[O_i$ (split)$]_{t=0}$ and not a factor of 10 as for the experimental ion fluences. At high values of $[O_i$ (split)$]_{t=0}$, the saturated $[O_i$ (oct)$^{2-}]_{t=\infty}$ becomes large enough to pin E_F at the deep acceptor states and only a very minor free electron concentration remains despite the back transfer O_i (oct)$^{2-}$ → O_i (split). Moreover, the saturation in $[O_i$ (oct)$^{2-}]$ takes place rather abruptly (Fig. 6), but this may be due to the simplicity of our model, omitting any influence by carrier diffusion and the nonuniform carrier concentration-versus-depth distribution.

In summary, the transformation between the O_i (split) and O_i (oct) configurations provides a semiquantitatively valid description of the experimental results. A fully quantitative agreement is more difficult and in particular, this holds for N_d (saturated loss) exhibiting no dependence on the ion fluence.

C. Migration of Zn_i and interaction with other defects and impurities

The Zn_i's induced by the cryogenic He$^+$ implantation, surviving recombination with the V_{Zn}'s (dynamic annealing), are anticipated to be mobile at RT and react with other defects and impurities. As discussed, reactions of Zn_i with the residual donor impurities Al_{Zn}, In_{Zn}, and H_O, do not cause any net effect on N_d, all being shallow donors. This is also true for interaction with Li_{Zn}, acting as acceptor with its state in the lower part of the band gap [38–40], where the resulting Li_i is a shallow donor. However, the negatively charged Li_{Zn}^- acceptor is likely to trap migrating Zn_i^{2+} donors because of the Coulomb attraction and the dominant Li concentration in the studied samples (Table I). In as-grown HT-ZnO samples of n type, the Li atoms reside almost exclusively on the substitutional Zn site as shown experimentally in Ref. [41], i.e., Li_{Zn} dominates strongly in our samples while the fraction of Li_i
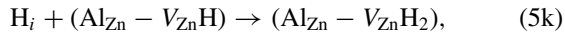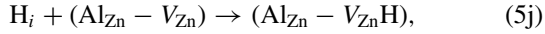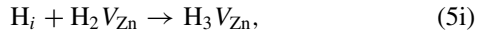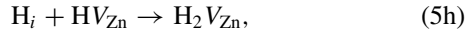
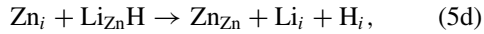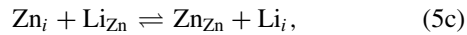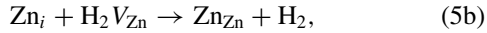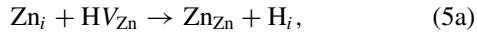and Li_i-Li_{Zn} pairs is negligible. The Li_{Zn} acceptors are readily passivated by residual H atoms, manifested by the prominent infrared absorption band at 3577 cm^{-1} arising from a local vibrational mode of an OH bond adjacent to Li_{Zn} [42–44]. FTIR measurements of our samples revealed a concentration of Li_{Zn}H centers of $(1.5 \pm 0.5) \times 10^{17}$ cm^{-3} adopting the absorption strength value given by Klauer *et al.* [45]. Thus, the vast majority of the Li_{Zn} acceptors are electrically passivated and where also compensation by shallow H_O donors can be significant, consistent with $N_d \approx 1 \times 10^{15}$ cm^{-3} and the Al_{Zn}/In_{Zn} donors being in the 10^{15} cm^{-3} range (cf. Table I).

Another obvious trap for the migrating Zn_i's is V_{Zn}, abundant in as-grown n-type samples because of the thermodynamics and with a uniform distribution after equilibration. Results from DFT calculations employing the HSE functional suggest a V_{Zn} formation energy of ∼0.5 eV in n-type samples with $N_d \approx 10^{15}$ cm^{-3} under O-rich ambient [7]. This translates into $[V_{Zn}]$ being on the order of 10^{15} cm^{-3} at 300 K under thermodynamic equilibrium, which is also corroborated by results from positron annihilation spectroscopy measurements [46] on similar type of samples as used in the present study. As found both experimentally and theoretically by several authors [47–51], the V_{Zn}'s interact strongly with H because of the large gain in total energy for $H_n V_{Zn}$ complexes (n is an integer number) relative to isolated V_{Zn}'s and H's. This is especially true for $n = 1$ and $n = 2$ leading to removal of electrons from the conduction band and where $H_2 V_{Zn}$ is a fully passivated (electrically neutral) defect. H_i is mobile already at RT [52–54] and the $H_n V_{Zn}$ complexes are, indeed, expected to form readily in HT samples containing a high amount of H (∼10^{17} cm^{-3} range). In a very recent FTIR absorption study by Herklotz *et al.* [51] using H-enriched samples prepared via in-diffusion, indication was also found for a $H_3 V_{Zn}$ complex and its thermodynamic stability was supported by first-principles theory calculations. Hence, in our samples isolated V_{Zn}'s are regarded to be scarce and the implantation-induced Zn_i's will predominantly interact with $H_n V_{Zn}$ complexes. In particular, $H_2 V_{Zn}$ is likely to prevail because of a lower formation energy than $(HV_{Zn} + H_i)$ by ∼2.7 eV [55] and $[H] \gg [V_{Zn}]$. Interestingly, the reaction $Zn_i^{2+} + H_2 V_{Zn}{}^0 \rightarrow Zn_{Zn} + H_2$ is energetically very favorable by ∼2.6 eV, as estimated by our DFT calculations, and causes also a reduction in N_d. Likewise, $H_3 V_{Zn}$ may play a role as trap for Zn_i^{2+} but $H_3 V_{Zn}$ is predicted to be donorlike [55] and Coulomb repulsion may suppress the probability for trapping.

A third type of interaction for the Zn_i's is with defects involving the donor impurities Al and In. A direct reaction between Zn_i^{2+} and the substitutional Al_{Zn}^+ donor is excluded because of the Coulomb repulsion and the same holds for In_{Zn}^+. In the following, only Al will be discussed since an analogous behavior is expected for In. As recently reported in the literature [56–58], Al_{Zn} tends to complex with V_{Zn} where the resulting $(Al_{Zn} - V_{Zn})$ defect is energetically stable with respect to the individual constituents and exhibits an overall acceptorlike character. Angular-dependent EPR measurements have revealed that the Al atom resides on a next-nearest neighbor Zn site to the V_{Zn} [58]. The latter accommodates most of the electron spin density yielding a g factor close to that of the isolated (nonaxial) V_{Zn}^-. The acceptor state of $(Al_{Zn} - V_{Zn})^-$ occurs in the lower part of the band gap and

in n-type samples, the reaction $Zn_i{}^{2+} + (Al_{Zn} - V_{Zn})^-$ is very likely, promoted by the Coulomb attraction. Further, because of the similar structure of V_{Zn} in the $(Al_{Zn} - V_{Zn})$ center and in its isolated form, also H passivation of $(Al_{Zn} - V_{Zn})$ can be expected giving rise to neutral $(Al_{Zn} - V_{Zn}H)$ centers. These centers will trap Zn_i's with a calculated energy gain of ~ 3.6 eV for the reaction $Zn_i{}^{2+} + (Al_{Zn} - V_{Zn}H)^0 \rightarrow Al_{Zn}{}^+ + Zn_{Zn} + H_i{}^+$. Moreover, it can be speculated about the existence of $(Al_{Zn} - V_{Zn}H_2)$ centers but they will most likely be positively charged restraining the trapping of $Zn_i{}^{2+}$.

On the basis of the discussion above, the following reactions are considered as the most crucial ones for the kinetics evolution of $Zn_i{}^{2+}$ in our samples:

$$Zn_i + HV_{Zn} \rightarrow Zn_{Zn} + H_i, \tag{5a}$$

$$Zn_i + H_2V_{Zn} \rightarrow Zn_{Zn} + H_2, \tag{5b}$$

$$Zn_i + Li_{Zn} \rightleftharpoons Zn_{Zn} + Li_i, \tag{5c}$$

$$Zn_i + Li_{Zn}H \rightarrow Zn_{Zn} + Li_i + H_i, \tag{5d}$$

$$Zn_i + (Al_{Zn} - V_{Zn}) \rightarrow Zn_{Zn} + Al_{Zn}, \tag{5e}$$

$$Zn_i + (Al_{Zn} - V_{Zn}H) \rightarrow Zn_{Zn} + Al_{Zn} + H_i, \tag{5f}$$

$$H_i + V_{Zn} \rightarrow HV_{Zn}, \tag{5g}$$

$$H_i + HV_{Zn} \rightarrow H_2V_{Zn}, \tag{5h}$$

$$H_i + H_2V_{Zn} \rightarrow H_3V_{Zn}, \tag{5i}$$

$$H_i + (Al_{Zn} - V_{Zn}) \rightarrow (Al_{Zn} - V_{Zn}H), \tag{5j}$$

$$H_i + (Al_{Zn} - V_{Zn}H) \rightarrow (Al_{Zn} - V_{Zn}H_2), \tag{5k}$$
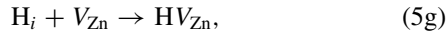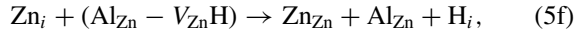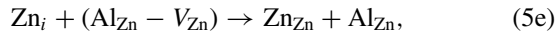
where Zn_i and H_i are mobile and the other species are regarded as immobile in the studied temperature range (290–325 K). Applying the theory for diffusion-limited reactions [59,60], the coupled differential rate equations given in Table II are derived from the reactions (5a)–(5k). Only the peak region around R_p is considered and concentration gradients are neglected due to the short diffusion lengths involved with no detectable broadening of the N_d profiles during annealing. The input values used for the different defects involving impurities are guided by the SIMS, FTIR, and CV data. The thermodynamic $[V_{Zn}]$ is taken as $\sim 8 \times 10^{14}$ cm^{-3} (cf. previous discussion), and because of the large energy gain, V_{Zn} is assumed to be decorated by the abundant H atoms (H_2V_{Zn} and H_3V_{Zn}) and partly to complex with the less abundant Al_{Zn} donors ($(Al_{Zn} - V_{Zn})$ and $(Al_{Zn} - V_{Zn}H)$). The diffusivity of Zn_i, D_{Zn_i}, is treated as a fitting parameter while that of H_i, D_{H_i}, is taken from Ref. [54]. Reaction (5b) is very favorable (energy gain ~ 2.6 eV) and determines N_d (loss) which equals $2 \times [H_2]$, accounting for the 2+ charge state of Zn_i. Also reaction (5d) exhibits a quite large energy gain (~ 1.8 eV) and due to the high $Li_{Zn}H$ concentration, large trapping of Zn_i may be expected. However, the interaction between Zn_i and Li_{Zn} invokes energy barriers where that of the kick-out reaction $Li_i + Zn_{Zn} \rightarrow Li_{Zn} + Zn_i$ is high with a calculated value of $\geqslant 1.6$ eV in n-type samples [61]. The barrier of the reverse (kick-in) reaction, which resembles our reactions (5c) (forward direction) and (5d), is low and estimated to be close to the migration energy of Zn_i within ~ 0.2 eV [62]. In the simulations, a small barrier of 0.2 eV has been included for the reactions (5c) (forward direction) and (5d) and actually, it

plays a significant role in reducing the trapping rate of Zn_i by $Li_{Zn}H$ (and Li_{Zn}) in the studied temperature range.

Here, it should be emphasized that the kick-in reactions (5c) (forward direction) and (5d) are found to have a crucial impact on the evolution of the concentration profiles of residual Li impurities during annealing of high-dose implanted HT-ZnO samples [63,64]. After implantation with Zn-substituting elements at RT and annealing at temperatures in the range of 600–800 °C, a large depletion of Li occurs beyond the implanted region (up to ~ 30 μm). This is attributed to the kick-in mechanism, arising from the release of Zn_i's trapped in the implanted region, followed by migration of Li_i's being highly mobile at the elevated annealing temperatures.

The differential rate equations in Table II have been solved numerically, and in Fig. 4(a), the simulated and experimental data for N_d (loss) are compared at 290, 300, 310, and 320 K annealing temperatures. A close quantitative agreement is obtained using D_{Zn_i} as fitting parameter, and the extracted D_{Zn_i} values are depicted in Fig. 4(b); an activation energy of ~ 0.75 eV is deduced, in good agreement with DFT estimates of ~ 0.5–0.8 eV for Zn_i migration parallel to the c axis [1,4]. The preexponential factor of D_{Zn_i}, D_0, exhibits a value of $\sim 10^{-3}$ cm^2/s, which is in the expected range for "ordinary" interstitial self-diffusion [65]. However, D_0 suffers from some uncertainty and cannot be determined independently using the present data. In a first approximation, the rate constant, c, for the loss of $[H_2V_{Zn}]$ (and thus N_d) is given by

$$c = 4\pi R D_{Zn_i}[Zn_i] = c_0 e^{-E_{migr}(Zn_i)/kT}, \tag{6}$$

with $c_0 = 4\pi R D_0[Zn_i]$. Hence, the individual contributions of D_0 and $[Zn_i]$ cannot be decomposed from c_0. For the D_0 value given in Fig. 4(b), $[Zn_i]_{t=0}$ was estimated from simulations using the SRIM code [14] with implantation conditions similar to the experimental ones (850 keV He$^+$ ions and fluences of 5×10^9 and 5×10^{10} cm^{-2}). Further, the threshold energy for displacement of Zn atoms (and O atoms) was put to 15 eV, a typical value for semiconductors [66–68]. The SRIM simulations do not account for dynamic annealing (recombination of vacancies and self-interstitials) during implantation, which is pronounced in ZnO [5], and 15% of the Zn_i's generated by the ballistic collisions were assumed to escape recombination during the implants performed at ~ 40 K. This gives $[Zn_i]_{t=0} = 3 \times 10^{15}$ cm^{-3} in the implantation peak region for the fluence of 5×10^9 He$^+$/cm^2 (3×10^{16} cm^{-3} for 5×10^{10} He$^+$/cm^2) and is a lower limit in order to reproduce the first-order kinetics of N_d (loss), i.e., $[Zn_i]_{t=0} \gg [H_2V_{Zn}]$. On the other hand, the upper limit of $[Zn_i]_{t=0}$ cannot exceed the concentration of ballistically generated Zn_i's, $\sim 2 \times 10^{16}$ cm^{-3} (5×10^9 He$^+$/cm^2 and no dynamic annealing), and thus, it can be inferred that D_0 is in the range of 10^{-4}–10^{-3} cm^2/s. In this context, it should be underlined that the recombination between Zn_i and V_{Zn} ($Zn_i + V_{Zn} \rightarrow \emptyset$) is considered to prevail during the dynamic annealing stage while being of less importance during the post-implant annealing described by the reactions (5a)–(5k).

In summary, the model of Zn_i migration and annihilation by H_2V_{Zn} centers as the central ingredient shows good quantitative agreement with all the experimental findings and the D_{Zn_i} values obtained are corroborated by DFT results.

TABLE II. Survey of the simultaneous differential rate equations for the reactions in Eqs. (5a)–(5k) and numerical values of the input parameters and concentrations used in the computations.

Simultaneous differential equations	$\frac{d[Zn_i]}{dt} = -4\pi R D_{Zn_i}[Zn_i]\{[H_2V_{Zn}] + e^{-E_{bar}/kT}\{[Li_{Zn}] + [Li_{Zn}H]\} + [(Al_{Zn} - V_{Zn}H)]\}$ $\quad -4\pi R_A D_{Zn_i}[Zn_i]\{[HV_{Zn}] + [(Al_{Zn} - V_{Zn})]\}$
	$\frac{d[V_{Zn}]}{dt} = -4\pi R_A D_{H_i}[H_i][V_{Zn}]$
	$\frac{d[HV_{Zn}]}{dt} = 4\pi R_A D_{H_i}[H_i]\{[V_{Zn}] - [HV_{Zn}]\}$
	$\frac{d[H_2V_{Zn}]}{dt} = -4\pi R D_{Zn_i}[Zn_i][H_2V_{Zn}] + 4\pi D_{H_i}[H_i]\{R_A[HV_{Zn}] - R[H_2V_{Zn}]\}$
	$\frac{d[H_3V_{Zn}]}{dt} = 4\pi R D_{H_i}[H_i][H_2V_{Zn}]$
	$\frac{d[H_i]}{dt} = 4\pi R D_{Zn_i}[Zn_i]\{e^{-E_{bar}/kT}[Li_{Zn}H] + [(Al_{Zn} - V_{Zn}H)]\}$ $\quad -4\pi D_{H_i}[H_i](R_A\{[V_{Zn}] + [HV_{Zn}] + [Li_{Zn}] + [(Al_{Zn} - V_{Zn})]\} + R\{[H_2V_{Zn}] + [(Al_{Zn} - V_{Zn}H)]\})$
	$\frac{d[H_2]}{dt} = 4\pi R D_{Zn_i}[Zn_i][H_2V_{Zn}]$
	$\frac{d[Li_{Zn}]}{dt} = -4\pi R_A D_{Zn_i}[Zn_i]e^{-E_{bar}/kT}[Li_{Zn}] - 4\pi R_A D_{H_i}[H_i][Li_{Zn}]$
	$\frac{d[Li_{Zn}H]}{dt} = -4\pi R D_{Zn_i}[Zn_i]e^{-E_{bar}/kT}[Li_{Zn}H] + 4\pi R_A D_{H_i}[H_i][Li_{Zn}]$
	$\frac{d[Li_i]}{dt} = 4\pi D_{Zn_i}[Zn_i]e^{-E_{bar}/kT}\{R_A[Li_{Zn}] + R[Li_{Zn}H]\}$
	$\frac{d[Al_{Zn}]}{dt} = 4\pi D_{Zn_i}[Zn_i]\{R_A[(Al_{Zn} - V_{Zn})] + R[(Al_{Zn} - V_{Zn}H)]\}$
	$\frac{d[(Al_{Zn}-V_{Zn})]}{dt} = -4\pi R_A\{D_{Zn_i}[Zn_i] + D_{H_i}[H_i]\}[(Al_{Zn} - V_{Zn})]$
	$\frac{d[(Al_{Zn}-V_{Zn}H)]}{dt} = 4\pi D_{H_i}[H_i]\{R_A[(Al_{Zn} - V_{Zn})] - R[(Al_{Zn} - V_{Zn}H)]\} - 4\pi R D_{Zn_i}[Zn_i][(Al_{Zn} - V_{Zn}H)]$
	$\frac{d[(Al_{Zn}-V_{Zn}H_2)]}{dt} = 4\pi R D_{H_i}[H_i][(Al_{Zn} - V_{Zn}H)]$
Capture radius	$R = 5$ Å, $R_A = 25$ Å (Coulomb attraction of H_i^+) and 50 Å (Zn_i^{2+})
Energy barrier	$E_{bar} = 0.2$ eV (energy barrier for Zn_i capture by Li_{Zn} and $Li_{Zn}H$)
Diffusivity	$D_{H_i} = 3 \times 10^{-4}e^{-0.6(eV)/kT}$ cm^2/s, taken from Ref. [54]
Initial values ($t = 0$) in cm^{-3}	$[Zn_i] = 3 \times 10^{15}$ (5×10^9 He$^+$/cm^2) and 3×10^{16} (5×10^{10} He$^+$/cm^2) $[V_{Zn}] = 3 \times 10^{15}$ (5×10^9 He$^+$/cm^2) and 3×10^{16} (5×10^{10} He$^+$/cm^2) $[V_{Zn}H] = 1 \times 10^{13}$, $[V_{Zn}H_2] = 3 \times 10^{14}$, $[V_{Zn}H_3] = 3 \times 10^{14}$ $[H_i] = [H_2] = [Li_i] = 0$ $[Li_{Zn}] = 5 \times 10^{15}$, $[Li_{Zn}H] = 1.7 \times 10^{17}$ $[Al_{Zn}] = 6 \times 10^{15}$, $[Al_{Zn} - V_{Zn}] = 5 \times 10^{13}$, $[Al_{Zn} - V_{Zn}H] = 5 \times 10^{13}$, $[Al_{Zn} - V_{Zn}H_2] = 5 \times 10^{13}$

V. CONCLUSIONS

In situ CV and junction spectroscopy measurements were applied to study *n*-type HT-ZnO samples implanted with low fluences of He$^+$ ions at ∼40 K. Only a minor reduction in N_d occurs immediately after implantation but a gradual decrease develops as a function of annealing temperature and time. The loss rate of N_d obeys first-order kinetics with an activation energy of ∼0.70 eV and a preexponential factor of ∼10^6 s^{-1}. The loss rate scales with the He fluence and evidences the role of implantation-induced elementary point defects, especially Zn_i and O_i. Moreover, the loss in N_d saturates at a certain value irrespective of the ion fluence used. The experimental data are supplemented by results from first-principles DFT calculations and from simulations of diffusion-limited defect reactions. Two models are put forward in order to explain the experimental data. One invokes transformation of O_i from the neutral split configuration to the double negatively charged octahedral configuration, and it shows semiquantitative agreement with the experiments. However, the saturation of N_d (loss) with no fluence dependence is challenging to reproduce fully. The other model invokes diffusion of Zn_i and trapping by residual H_2V_{Zn} centers as the key feature. This model exhibits good quantitative agreement with all the experimental observations and it gives an activation energy for Zn_i migration of ∼0.75 eV, consistent with previous DFT estimates in the literature.

[1] A. Janotti and C. G. Van de Walle, Phys. Rev. B **76**, 165202 (2007).

[2] Y. V. Gorelkinskii and G. D. Watkins, Phys. Rev. B **69**, 115212 (2004).

[3] L. S. Vlasenko and G. D. Watkins, Phys. Rev. B **72**, 035203 (2005).

[4] P. Erhart and K. Albe, Appl. Phys. Lett. **88**, 201918 (2006).

[5] S. O. Kucheyev, J. S. Williams, C. Jagadish, J. Zou, C. Evans, A. J. Nelson, and A. V. Hamza, Phys. Rev. B **67**, 094115 (2003).

[6] E. V. Monakhov, A. Yu. Kuznetsov, and B. G. Svensson, J. Phys. D **42**, 153001 (2009).

[7] F. Oba, A. Togo, I. Tanaka, J. Paier, and G. Kresse, Phys. Rev. B **77**, 245202 (2008).

[8] A. Janotti and C. G. Van de Walle, Rep. Prog. Phys. **72**, 126501 (2009).

[9] L. Vines, J. Wong-Leung, C. Jagadish, V. Quemener, E. V. Monakhov, and B. G. Svensson, Appl. Phys. Lett. **100**, 212106 (2012).

[10] F. D. Auret, S. A. Goodman, M. Hayes, M. J. Legodi, H. A. van Laarhoven, and D. C. Look, Appl. Phys. Lett. **79**, 3074 (2001).

[11] M. Hayes, F. D. Auret, P. J. J. van Rensburg, J. M. Nel, W. Wesch, and E. Wendler, Phys. Status Solidi B **244**, 1544 (2007).

[12] M. Hayes, F. Auret, P. J. van Rensburg, J. Nel, W. Wesch, and E. Wendler, Nucl. Instrum. Methods Phys. Res., Sect. B **257**, 311 (2007).

[13] Z.-Q. Fang, B. Claflin, D. C. Look, and G. C. Farlow, J. Appl. Phys. **101**, 086106 (2007).

[14] J. F. Ziegler, M. Ziegler, and J. Biersack, Nucl. Instrum. Methods Phys. Res., Sect. B **268**, 1818 (2010).

[15] A. A. Istratov, J. Appl. Phys. **82**, 2965 (1997).

[16] P. E. Blöchl, Phys. Rev. B **50**, 17953 (1994).

[17] J. P. Perdew, K. Burke, and M. Ernzerhof, Phys. Rev. Lett. **77**, 3865 (1996).

[18] G. Kresse and J. Hafner, Phys. Rev. B **47**, 558 (1993).

[19] G. Henkelman, B. P. Uberuaga, and H. Jónsson, J. Chem. Phys. **113**, 9901 (2000).

[20] J. Heyd, G. E. Scuseria, and M. Ernzerhof, J. Chem. Phys. **118**, 8207 (2003).

[21] Y. Kumagai and F. Oba, Phys. Rev. B **89**, 195205 (2014).

[22] C. Freysoldt, J. Neugebauer, and C. G. Van de Walle, Phys. Rev. Lett. **102**, 016402 (2009).

[23] L. C. Kimerling, J. Appl. Phys. **45**, 1839 (1974).

[24] N. T. Son, X. T. Trinh, L. S. Løvlie, B. G. Svensson, K. Kawahara, J. Suda, T. Kimoto, T. Umeda, J. Isoya, T. Makino, T. Ohshima, and E. Janzén, Phys. Rev. Lett. **109**, 187603 (2012).

[25] R. Schifano, E. V. Monakhov, L. Vines, B. G. Svensson, W. Mtangi, and F. D. Auret, J. Appl. Phys. **106**, 043706 (2009).

[26] A. Hupfer, C. Bhoodoo, L. Vines, and B. G. Svensson, Appl. Phys. Lett. **104**, 092111 (2014).

[27] W. Mtangi, M. Schmidt, F. D. Auret, W. E. Meyer, P. J. J. van Rensburg, M. Diale, J. M. Nel, A. G. M. Das, F. C. C. Ling, and A. Chawanda, J. Appl. Phys. **113**, 124502 (2013).

[28] T. Frank, G. Pensl, R. Tena-Zaera, J. Zúñiga-Pérez, C. Martínez-Tomás, V. Muñoz-Sanjosé, T. Ohshima, H. Itoh, D. Hofmann, D. Pfisterer, J. Sann, and B. Meyer, Appl. Phys. A **88**, 141 (2007).

[29] M. Ellguth, M. Schmidt, R. Pickenhain, H. V. Wenckstern, and M. Grundmann, Phys. Status Solidi B **248**, 941 (2011).

[30] V. Quemener, L. Vines, E. V. Monakhov, and B. G. Svensson, Appl. Phys. Lett. **100**, 112108 (2012).

[31] B. G. Svensson and J. L. Lindström, Phys. Rev. B **34**, 8709 (1986).

[32] L. S. Løvlie and B. G. Svensson, Phys. Rev. B **86**, 075205 (2012).

[33] B. K. Meyer, H. Alves, D. M. Hofmann, W. Kriegseis, D. Forster, F. Bertram, J. Christen, A. Hoffmann, M. Straßburg, M. Dworzak, U. Haboeck, and A. V. Rodina, Phys. Status Solidi B **241**, 231 (2004).

[34] A. Janotti and C. G. Van de Walle, Nat. Mater. **6**, 44 (2006).

[35] J. W. Corbett, in *Electron Radiation Damage in Semiconductors and Metals*, edited by F. Seitz and D. Turnbull (Academic, New York, 1966).

[36] W. Shockley and W. T. Read, Phys. Rev. **87**, 835 (1952).

[37] R. N. Hall, Phys. Rev. **87**, 387 (1952).

[38] C. H. Park, S. B. Zhang, and S.-H. Wei, Phys. Rev. B **66**, 073202 (2002).

[39] M. G. Wardle, J. P. Goss, and P. R. Briddon, Phys. Rev. B **71**, 155205 (2005).

[40] M. D. McCluskey and S. J. Jokela, J. Appl. Phys. **106**, 071101 (2009).

[41] L. Vines, E. V. Monakhov, R. Schifano, W. Mtangi, F. D. Auret, and B. G. Svensson, J. Appl. Phys. **107**, 103707 (2010).

[42] L. E. Halliburton, L. Wang, L. Bai, N. Y. Garces, N. C. Giles, M. J. Callahan, and B. Wang, J. Appl. Phys. **96**, 7168 (2004).

[43] E. V. Lavrov, F. Börrnert, and J. Weber, Phys. Rev. B **71**, 035205 (2005).

[44] G. A. Shi, M. Stavola, and W. B. Fowler, Phys. Rev. B **73**, 081201 (2006).

[45] S. Klauer, M. Wöhlecke, and S. Kapphan, Phys. Rev. B **45**, 2786 (1992).

[46] F. Tuomisto, V. Ranki, K. Saarinen, and D. C. Look, Phys. Rev. Lett. **91**, 205502 (2003).

[47] E. V. Lavrov, J. Weber, F. Börrnert, C. G. Van de Walle, and R. Helbig, Phys. Rev. B **66**, 165205 (2002).

[48] M. G. Wardle, J. P. Goss, and P. R. Briddon, Phys. Rev. B **72**, 155108 (2005).

[49] F. Herklotz, E. V. Lavrov, V. Kolkovsky, J. Weber, and M. Stavola, Phys. Rev. B **82**, 115206 (2010).

[50] D. Bastin, E. V. Lavrov, and J. Weber, Phys. Rev. B **83**, 195210 (2011).

[51] F. Herklotz, A. Hupfer, K. M. Johansen, B. G. Svensson, S. G. Koch, and E. V. Lavrov, Phys. Rev. B **92**, 155203 (2015).

[52] M. G. Wardle, J. P. Goss, and P. R. Briddon, Phys. Rev. Lett. **96**, 205504 (2006).

[53] K. M. Johansen, J. S. Christensen, E. V. Monakhov, A. Yu. Kuznetsov, and B. G. Svensson, Appl. Phys. Lett. **93**, 152109 (2008).

[54] A. Hupfer, C. Bhoodoo, L. Vines, and B. G. Svensson, J. Appl. Phys. **119**, 181506 (2016).

[55] A. Hupfer, B. G. Svensson, and C. Persson, Hydrogen decorated cation vacancies in gan, gap, zno and zns: Stabilization by self-passivation (unpublished).

[56] J. T-Thienprasert, S. Rujirawat, W. Klysubun, J. N. Duenow, T. J. Coutts, S. B. Zhang, D. C. Look, and S. Limpijumnong, Phys. Rev. Lett. **110**, 055502 (2013).

[57] J.-Y. Noh, H. Kim, Y.-S. Kim, and C. H. Park, J. Appl. Phys. **113**, 153703 (2013).

[58] J. E. Stehr, K. M. Johansen, T. S. Bjørheim, L. Vines, B. G. Svensson, W. M. Chen, and I. A. Buyanova, Phys. Rev. Appl. **2**, 021001 (2014).

[59] T. R. Waite, Phys. Rev. **107**, 463 (1957).

[60] T. R. Waite, J. Chem. Phys. **28**, 103 (1958).

[61] G.-Y. Huang, C.-Y. Wang, and J.-T. Wang, J. Phys.: Condens. Matter **21**, 345802 (2009).

[62] A. Carvalho, A. Alkauskas, A. Pasquarello, A. K. Tagantsev, and N. Setter, Phys. Rev. B **80**, 195205 (2009).

[63] P. T. Neuvonen, L. Vines, B. G. Svensson, and A. Yu. Kuznetsov, Phys. Rev. Lett. **110**, 015501 (2013).

[64] A. Yu. Azarov, K. E. Knutsen, P. T. Neuvonen, L. Vines, B. G. Svensson, and A. Yu. Kuznetsov, Phys. Rev. Lett. **110**, 175503 (2013).

[65] J. Philibert, *Atom Movements: Diffusion and Mass Transport in Solids* (Les Editions de Physique, Les Ulis, France, 1991).

[66] J. J. Loferski and P. Rappaport, Phys. Rev. **111**, 432 (1958).

[67] B. G. Svensson and J. L. Lindström, J. Appl. Phys. **72**, 5616 (1992).

[68] B. G. Svensson, C. Jagadish, A. Hallén, and J. Lalita, Phys. Rev. B **55**, 10498 (1997).